Unraveling the reversible formation of defective Ce3+sites in the UiO-66(Ce) material: a multi-technique study

Unraveling the reversible formation of defective Ce^{3+} sites in the UiO-66(Ce) material: a multi-technique study

Sergio Rojas-Buzo [a*], Davide Salusso [a], Francesca Bonino [a], Maria Cristina Paganini [a] and Silvia Bordiga [a*]

[a] Department of Chemistry, NIS and INSTM Reference Centre, Università di Torino, 10125, Italy.

Abstract

Ce^{3+} presence and formation in Ce-based UiO-66 Metal Organic Framework (MOF) still presents a debated evaluation between the employed characterization techniques. In this work, we have prepared a defective UiO-66(Ce) and investigated the nature of Ce^{3+} sites on the CeO_x clusters. Laboratory techniques (EPR, XPS, UV-Vis and FTIR spectroscopy) were compared with *operando* Ce M_5-edge NEXAFS to study Ce^{3+} accessibility. All the employed techniques presented different degrees of accessibility or reliability (e.g., sample damage or not sufficient sensitivity). Among the obtained results, EPR, UV-Vis and NEXAFS spectroscopies unraveled $Ce^{4+}\rightarrow Ce^{3+}$ conversion during the sample dehydration. The MOF structure was not damaged by neither water loss nor the beam, directly relating Ce oxidation state to the water content, opening a new route to both synthesis of stable and active MOFs and non-invasive characterization strategies. Finally, laboratory measurements considerations were exploited for studying Ce^{3+} formation in Zr-doped UiO-66(Ce) samples.

Graphical abstract

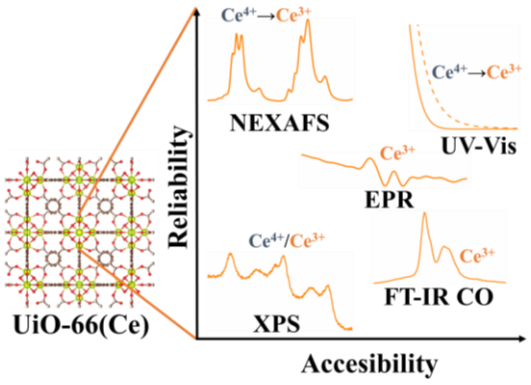

Keywords

MOF; UiO-66(Ce); Defective Site; Ce^{3+}; Multi-technique Characterization; NEXAFS

1. Introduction

Metal-organic frameworks (MOFs) are a class of crystalline materials characterized by a high structural versatility, which allows them to be designed and synthesized with high surface areas, tunable pore sizes and permanent porosity.[1–4] Unfortunately, some MOFs present limitations due to their poor stability, which limits their practical applications.[5,6] In this sense, tetravalent Zr-MOFs have been identified as having superior chemical, thermal and mechanical stability.[7–10] Concretely, the first Zr-based MOF reported was the UiO-66 (UiO stands for University of Oslo),[11] whose 3D structure consists in terephthalate ligands connected by secondary building units (SBUs) of $Zr_6O_4(OH)_4$ leading to a face-centered cubic (*fcu*) topology.[12]

In the last years, Ce(IV) has also been used to synthesize MOFs with identical topologies to those reported for the Zr-MOFs,[13,14] but with compromised chemical, thermal and mechanical stability compared to the Zr-based counterpart.[15–18] Ce special electronic property[19] could be employed to prepare MOF-based redox catalysts because of the relatively high abundance and low cost of Ce and the inherent switching tendency between Ce^{4+} and Ce^{3+}. In fact, since in 2015 Lammert et al.[20] reported the first synthesis of UiO-66(Ce), several groups have reported the importance of having this redox couple on the cluster for application in oxidative catalytic reactions,[21–23] supercapacitors[24] and for colorimetric sensing[25], among others. However, and despite its growing in this research field, the presence and the nature of the reduced Ce^{3+} species in the subnanometric clusters of MOFs is still unknown and just has been tentatively described by different spectroscopic techniques including access-limited ones, i.e., X-Ray Absorption Spectroscopy (XAS)[26] or more invasive such as X-Ray Photoelectron Spectroscopy (XPS),[27] where Ce sites can be partially reduced during the measurement.[28] Since to unravel the redox properties of the Ce-MOFs materials is necessary to know the character of their oxidized and reduced species, we have focused in understanding the nature and the amount of the Ce^{4+}/Ce^{3+} species and how they are generated on the UiO-66(Ce) clusters through different hand able spectroscopic techniques including FT-IR, Electron Paramagnetic Resonance (EPR) and UV-Vis and more advanced as NEXAFS. The results obtained for pure UiO-66(Ce) sample were then used for interpretation of results over UiO-66(Ce/Zr) materials discussed in the last part of the present manuscript.

2. Experimental section

2.1. Synthesis of MOFs

The UiO-66($Ce_{1-x}Zr_x$) compounds were synthesized using Pyrex glass vessel reactor (maximum volume 14 mL). Terephthalic acid (H_2BDC, 255.2 mg) and *N*,*N*-dimethylformamide (DMF, 6.8 g) were transferred into the glass reactor. Subsequently, formic acid (HCOOH, 100 %, 2.51 g) and a known amount of aqueous solutions of $(NH_4)_2Ce(NO_3)_6$ (0.296 g/g) and $ZrO(NO_3)_2{\cdot}H_2O$ (0.125 g/g) was added to reach the desired Ce:Zr stoichiometry (see Table 1 for details). The pure UiO-66(Ce) was synthesized in a similar way. Terephthalic acid (H_2BDC, 255.2 mg) and *N*,*N*-dimethylformamide (DMF, 8.5 g) were transferred into the glass reactor. Subsequently, 3 g of an aqueous solution of $(NH_4)_2Ce(NO_3)_6$ (0.296 g/g) were added. The glass reactors were heated under stirring for 15 min at 100 °C in an oil bath equipped with a thermocouple. After the synthesis, the glass reactors were cooled down to room temperature and the precipitates were isolated by centrifugation. The mother liquor solutions were decanted off and the MOFs were re-dispersed and centrifuged two times in DMF and two times in acetone. Finally, the samples were dried in an oven at 80ºC during 1 hour in order to remove the residual solvent molecules.

Table 1. Amount of Ce and Zr solutions employed for the synthesis of the UiO-66($Ce_{1-x}Zr_x$) materials

Sample	Ce solution (g)	Zr solution (g)
UiO-66($Ce_{0.5}Zr_{0.5}$)	1.77	0.61
UiO-66($Ce_{0.05}Zr_{0.95}$)	0.21	2.20

2.2. Characterization techniques

2.2.1. Standard characterization

The XRD measurements have been carried out using the Bragg–Brentano geometry with a PANalytical PW3050/60 X'Pert PRO MPD diffractometer with a Cu anode (Kα = 1.5418 Å) and an X'Celerator detector. Thermogravimetric analysis (TGA) data were recorded with a TA Instruments Q600 thermobalance in air flow (100 mL/min) with a ramp of 5 °C/min from RT to 600°C working with about 5 mg of sample in an alumina crucible. Isothermal N_2 physisorption measurements at liquid nitrogen temperature were performed on a Micromeritics ASAP 2020. Prior to the measurement, the powders were degassed overnight at 120 °C. Specific surface areas using the Brunauer–Emmett–Teller model were calculated following the Rouquerol´s criterion. Pore size distribution was obtained by applying the N_2-Cylindrical Pores-Oxide Surface DFT model.

2.2.2. Infrared spectroscopy

Fourier Transform Infrared (FTIR) spectroscopy in transmission mode was instead employed to characterize surface properties of the materials by following the adsorption/desorption of CO used as probe molecule. Absorption/transmission FTIR spectra were collected using a Bruker Vertex 70 spectrophotometer equipped with a Mercury Cadmium Telluride (MCT) cryo-detector in the 4000–600 cm^{-1} range with 2 cm^{-1} resolution. Powders were pressed in self-supporting discs (~4 mg/cm^2) and placed in quartz IR cells suitable for thermal treatments in controlled atmosphere and for spectra recording at liquid nitrogen temperature (nominal LNT). Before IR measurements, catalysts were activated from RT to 110 °C at 5 °C/min holding at 110 °C for 2h. Spectra were treated using Bruker OPUS spectroscopy software. The reported spectra of CO desorption were normalized to pellet mass and area.

2.2.3. UV-Vis Diffuse Reflectance Spectroscopy (DRS)

DR UV–Vis spectra were measured with a Varian Cary5000 spectrophotometer, equipped with a diffuse reflectance sphere. The samples were measured in powder form, in a homemade cell with a window in optical quartz (suprasil), which allows performing treatments in a vacuum and/or in the presence of gases. The materials were measured as-prepared, after an activation process at 110ºC under dynamic vacuum and after be re-exposed to the atmosphere when they were pretreated. The spectra were collected in a reflectance mode and successively converted as Kubelka–Munk F(R) function.

2.2.4. Electron Paramagnetic Resonance (EPR)

EPR experiments were run on a CW-EPR Bruker EMX spectrometer operating at X-band (9.5 GHz), equipped with a cylindrical cavity operating at 100 kHz field modulation. Spectra at 77 K were obtained by keeping the sample in liquid nitrogen using a finger Dewar set in the EPR cavity. The O_2 adsorption experiments were performed in EPR cells that previously were connected to high vacuum systems. O_2 adsorption was carried out after an activation process of the samples at 110ºC during ~2h under dynamic vacuum. For all the experiments, 10 mbar of oxygen was dosed in the EPR cell at room temperature, and then the temperature was lowered to 77 K by immersion in liquid nitrogen.

2.2.5. X-Ray Photoelectron Spectroscopy (XPS)

XPS spectra were collected on a SPECS spectrometer equipped with a 150 MCD-9 detector and a non-monochromatic MgKα (1253.6 eV) X-ray source. Spectra were recorded with 30 eV analyzer pass, an X-ray power of 50 W and under

an operating pressure of 10−9 mbar. During data processing of the XPS spectra, binding energy (BE) values were referenced to C 1s peak (284.8 eV). Spectra treatment has been performed using the CASA software. Ce (3d) peak were fit using 6 and 4 Gaussian-Lorentzian (50:50) functions for Ce^{4+} and Ce^{3+} species, respectively. Spin-orbit splitting (Δ_{s-o}=18.5 eV) was used to constrain peaks position whilst spin-orbit couples were forced to the same FWHM values. Spline Shirley function was employed to describe background.

2.2.6. Ambient Pressure Near Edge X-Ray Absorption Spectroscopy (AP-NEXAFS)

AP-NEXAFS spectra were measured at APE-HE beamline of the Elettra Italian Synchrotron radiation source. Ce-UiO66 sample was placed in a specially designed reactor cell allowing thermal treatments in the RT-400°C range under a 1 bar gas atmosphere.[29–31] TEY mode was used to record the experimental spectra. Ce M_5 spectra were collected from 880 to 910 eV with 0.01 eV energy resolution. The sample heating (RT-110°C) was provided by an electric resistance while He (99.99999%) stream (50 mL/min) was kept constant during the measurement. Spectra were energy aligned to a reference CeO_2 measured simultaneously with the Ce-UiO66 sample. Thorondor software was employed for background subtraction and intensity normalization.[32] A 6^{th} order polynomial was used for background subtraction. Ce^{3+}/Ce^{4+} spectral pure components and their concentration evolution were extracted using MCR-ALS implemented in MATLAB with 99.5% of variance explained.[33] Spectra and concentration was constrained to positive values whilst closure condition was applied to concentrations.

3. Results and discussion

3.1. Synthesis and general characterization

The UiO-66(Ce) material studied in this work has been synthesized following a previous receipt described in the literature.[20] The resultant sample shows the characteristic PXRD pattern of the UiO-66 *fcu*-type structure (see Figure S1). However, in the low 2θ region, a very broad peak was detected in the pure UiO-66(Ce) (see Figure 1). The diffractions at 2-7º are attributed to the 100 and 110 reflections of the *reo* topology of UiO-66 and the intensity of these *reo* reflections is correlated with the concentration of missing cluster defects.[34,35] The presence and number of structural defects in the UiO-66, in this case cluster missing defects, depends on several factors including the pH of the mother solution, the presence of modulators and the reaction temperature, among others.[36] In our case, the possible degradation of DMF during the synthesis to produce formic acid causes a decrease on the pH value.[37] This

fact disfavors the ligand deprotonation and therefore its interaction with the Ce clusters, so more cluster missing defects are formed.

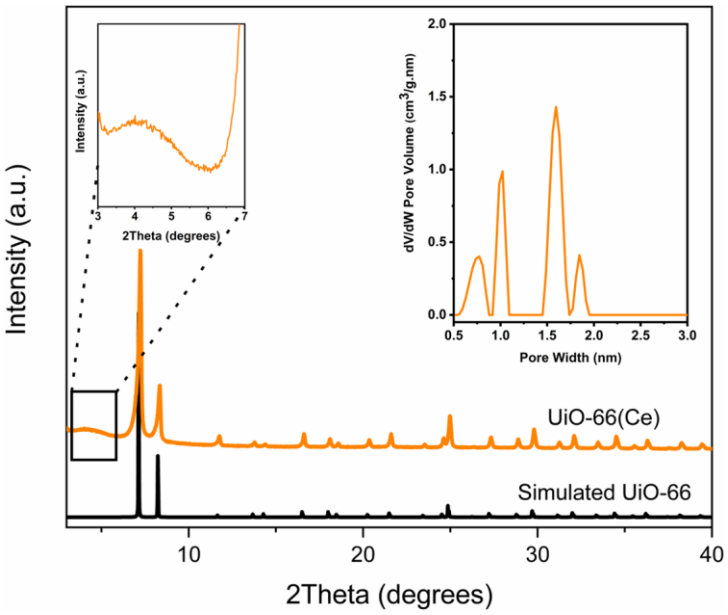

Figure 1. PXRD patterns of the simulated UiO-66(Ce) (black line) and as-synthesized UiO-66(Ce) (orange line). Pore size distribution of the UiO-66(Ce) material is reported in the right side inset.

We have also determined the thermal stability of the Ce-MOF by thermogravimetric analysis (see Figure S2). The TGA curve indicates that the UiO-66 framework is stable in air up to 300 ºC. Finally, the textural properties of the MOF were measured by N_2 adsorption isotherm. Type I isotherm was observed, which is characteristic of microporous materials (see Figure S3). The calculated BET area for the UiO-66(Ce) material synthesized in this work (~1132 m^2/g) is comparable to those previously reported for well-crystallized UiO-66-type materials.[11,22] The pore size distribution obtained by applying a DFT model (see experimental section and Figure S4 for more details) was shown in the inset of Figure 1. The classical *fcu* topology distribution, based on two different pore size (0.8 and 1.1 nm), is presented in the sample.[38] Moreover, a contribution of 1.8 nm pore is observed, which corresponds to the UiO-66 with missing cluster in the *reo* topology.[39] This *reo* topology creation is in accordance with the XRD findings.

3.2. Ce^{3+} formation in the UiO-66(Ce) material: a multi-technique study

FTIR spectra of CO adsorption has been employed to investigate the chemical nature of surface Ce sites (see Figure 2), available in particular in the case of defective samples. In fact, in an ideal 12-connected building unit we do not expect to have accessible Ce sites. First, we have analyzed the high frequency range since the different nature on the hydroxyl groups that could be achieved (see Figure 2, left panel). In the IR spectrum of pure UiO-66(Ce) activated (110°C, 5E-04 mbar), the band at 3645 cm^{-1} is assigned to the ν(OH) stretching mode of (μ_3-OH)Ce_6 cluster (see Figure 2, left panel, red spectrum).[40] The other peaks and shoulders observed in the ν(OH) region could be ascribed to the -OH/-OH_2 generated on the Ce cluster during the missing linker process. When CO was introduced in the cell at nominal Liquid Nitrogen Temperature (LNT), the ν(OH) stretching bands were substantially consumed whilst a broader band associated to interacting -OH groups was parallelly formed at ~3563 cm^{-1} (see Figure 2, left panel). At the highest CO coverage, two minor components at lower frequency with respect to the 3645 cm^{-1} band are still present, testifying this fraction of sites are not accessible to CO.

On the other hand, we have focused on the CO region to better unravel the nature of the Ce sites (Figure 2, right panel). The observed intense band at 2153 cm^{-1} follows the same (opposite) kinetic of the ν(OH) components, confirming the band association to CO-OH interaction.[41,42] Contrarily, for frequency position and formation stability at higher pressures, the band at 2136 cm^{-1} was related to physisorbed CO.[43] Moreover, even though the observed band at 2127 cm^{-1} is often ascribed to the CO-Ce^{3+} interaction,[44] its kinetic is very similar with the one at 2153 cm^{-1} (CO-OH) making this assignment not trivial. Conversely, there is not clear evidence of the presence of Ce^{4+}-CO adducts (band at 2173 cm^{-1}),[22] since the tails observed at both sides of the major components, are due to the tails of hindered rotators inside the MOF cages.

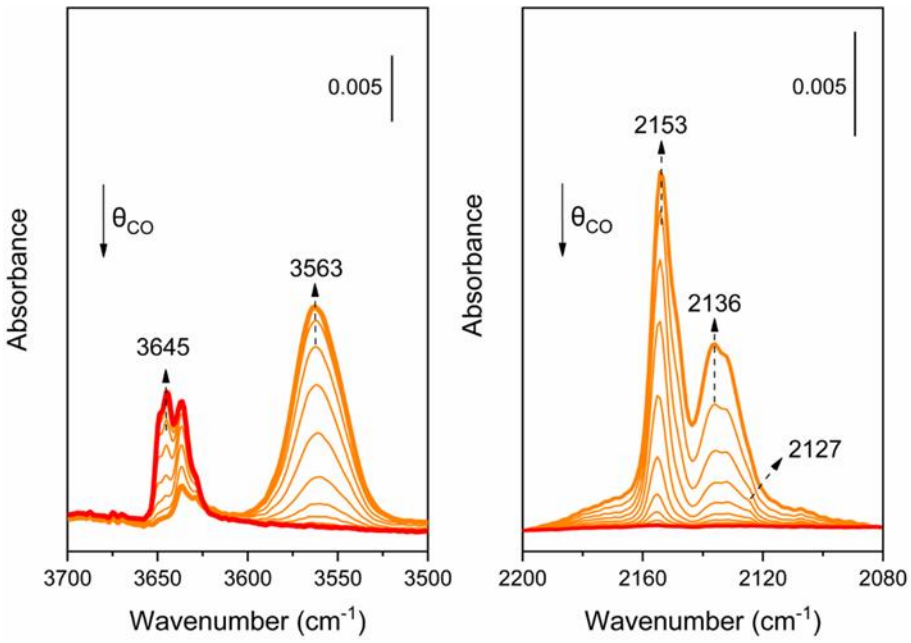

Figure 2. FT-IR spectra of CO desorption at LNT on UiO-66(Ce) focused on OH (left panel) and CO (right panel) regions.

UV-Vis Diffuse Reflectance Spectroscopy (DRS) experiments reported in Kubelka–Munk units in Figure 3 show a broad band between 350 and 500 nm assigned to a ligand-to-metal charge transfer i.e., from the 2p valence band of O^{2-} to the 4f levels, empty localized states, belonging to Ce^{4+}.[45] After sample activation (110°C, 5E-04 mbar), the absorption edge presented a slight red-shift which was previously assigned to Ce^{3+} and oxygen vacancies increment,[46–48] suggesting a Ce^{4+} partial reduction during the dehydration (even with the possible removal of neutral OH, O^{-} and O atom from the cluster to generate Ce^{3+} species). The decrease on the band gap from ~2.9 to ~2.7 eV is associated with an increase in the Ce^{3+} concentration (see Figure S5).[49] Interestingly, the absorption edge was blue-shifted after further exposure to air (Figure 3) highlighting a reversible redox character of the metallic clusters.

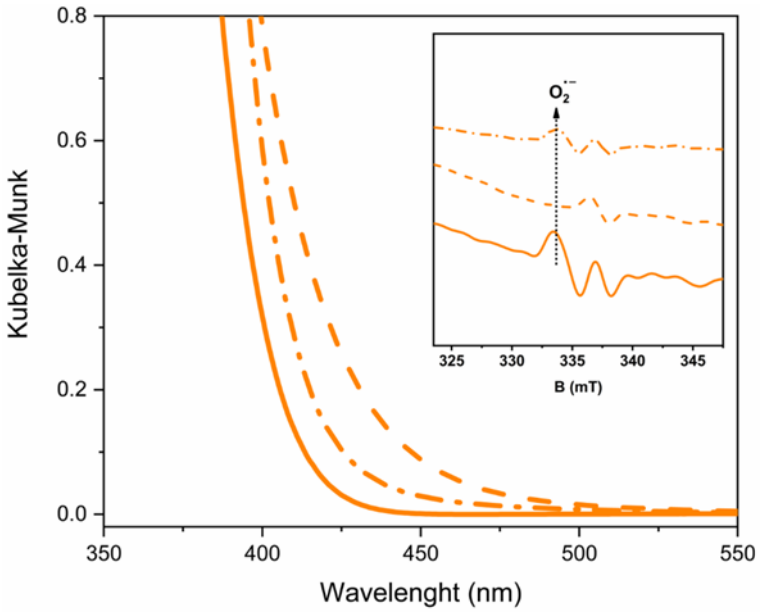

Figure 3. DRS UV-Vis spectra of the as-synthesized (solid line), activated at 110ºC (dash line) and re-exposed to the atmosphere (dash dot line) UiO-66(Ce) material. EPR spectra recorded at 77K of the UiO-66(Ce) material previously activated at 110ºC under dynamic vacuum and then exposed to 10 mbar of O_2 (solid line), after outgassing at room temperature (dash line) and after re-adsorption of 10 mbar of O_2 (dash dot line) are reported in the inset.

The presence of paramagnetic Ce^{3+} ions cannot be directly monitored by EPR because of different reasons: first Ce^{3+} is EPR silent due to its low relaxation time,[50] secondly in the temperature range covered by our experiments it is almost impossible to observe any cerium ions signal, finally because of the strong spin-orbit interactions occurring in the case of f-orbitals a strong heterogeneity of the g tensor is expected and for this reason a very broad and spread signal is present but impossible to be detected. Indeed, even if is not observable Ce^{3+} ions, their existence can be probed indirectly by the formation of superoxide $O_2^{\bullet-}$ species. After contacting the activated UiO-66(Ce) material with oxygen, a signal from $O_2^{\bullet-}$ was observed at ~333 mT and in the region of g values about 2.025 in the EPR spectrum, unveiling the presence of Ce^{3+} based on the following reaction (Figure 3 inset). [51,52]

$$O_2\ (gas) + Ce^{3+}\ (surf) \rightarrow O_2^{\bullet-} - Ce^{4+}\ (surf)$$

Interaction with O_2 was reversible since the observed signal was consumed and re-formed after a consequent O_2 desorption/re-adsorption cycle (Figure 3 inset). Generally, the formation of superoxide species on a cation site is a chemical reaction so irreversible, in the case of cerium ions we can observe a physisorption of molecular oxygen forming a reversible surface interaction.

Ce^{3+} quantification was further on attempted by Ce(3d) XPS spectra fitting. As observed in Figure S6, Ce^{3+}≈5% was estimated for UiO-66(Ce) sample. Moreover, it should be noticed as even though XPS is commonly used for Ce^{3+} quantification, it is also well reported as this type of band deconvolution can lead to several errors.[28] For instance, even though constrains have been applied to the fit (see SI), half of the Ce^{3+} bands were too weak to be visible, suggesting as the estimated Ce^{3+} concentration might be resulting from charging effects. Indeed, UiO-66(Ce) *operando* Total Electron Yield (TEY) Ce M_5-edge Near Edge X-ray Absorption Fine Structure (NEXAFS) spectra in Figure 4a showed as the as-prepared sample presented only Ce^{4+} spectra with fingerprints as 895 and 899 eV, whilst Ce^{3+} signal at 892 and 893 eV started to be visible during thermal activation. Due to the complex band convolution, MCR-ALS was applied to the reported dataset to extract Ce^{4+}/Ce^{3+} pure spectral components and concentration profiles (Figure 4b). The obtained spectral components were in good agreement with those measured from reference CeO_2 and CeF_3 (Figure S7) suggesting the successful exploitation of MCR-ALS routine. Moreover, the evaluated concentrations showed as Ce^{3+} increased (≈9%) during the first 30' of degassing at 25°C/He and raised to 40% during heating to 110°C. Ce^{4+} was almost fully recovered (Ce^{3+}≈12%) after further exposure to air (Figure 4a inset), ultimately confirming the relation between Ce^{3+} formation and UiO-66(Ce) dehydration.

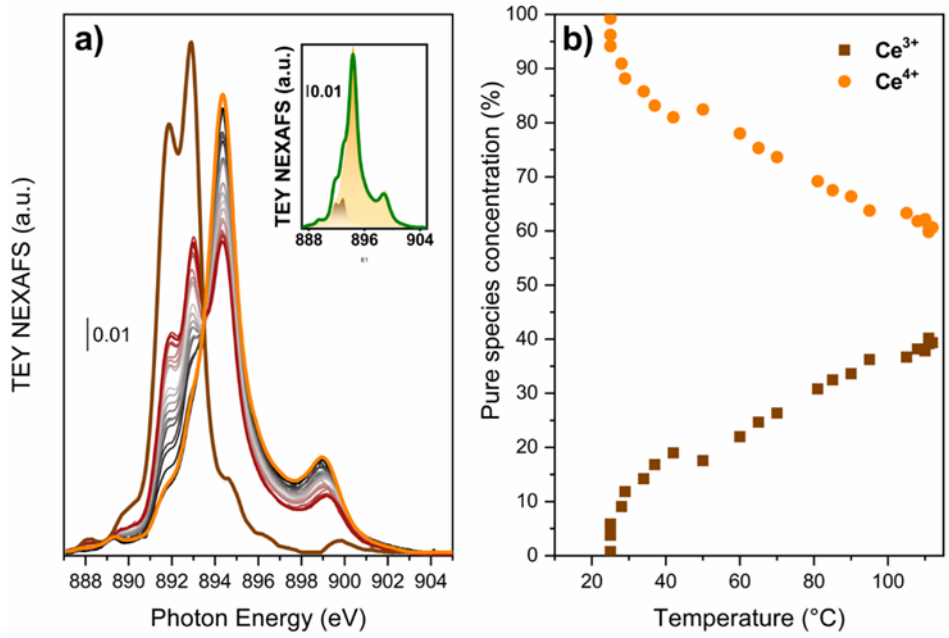

Figure 4. a) Ce M_5-edge NEXAFS spectra measured in TEY mode in the RT-110°C range under He flow. Temperature increases from black to red curve. Ce^{4+} and Ce^{3+} pure spectral component extracted by MCR-ALS are showed in orange and brown colours respectively. Spectra of UiO-66(Ce) measured after activation and further

exposure to air is reported in the inset (green curve). Weighted Ce^{4+} and Ce^{3+} components are indicated in orange and brown, respectively. b) Ce^{3+} (brown squares) and Ce^{4+} (orange circles) components concentration evolution with temperature.

This result, even though of difficult accessibility due to the use of synchrotron radiation, confirmed as laboratory measurements such as UV-Vis and CO adsorption FT-IR spectroscopies can led to the same qualitative information without accessing species quantification.

3.3. Zr-doping effect on the Ce^{3+} nature: corroborating the potential of the laboratory techniques

In order to verify the potential of laboratory measurement towards Ce^{3+} evaluation, we have prepared and applied the aforementioned consideration to Zr-doped UiO-66(Ce), commonly known to introduce Ce atoms on the ZrO_x clusters.[53] UiO-66(Ce/Zr) samples denoted as UiO-66($Ce_{0.5}Zr_{0.5}$) and UiO-66($Ce_{0.05}Zr_{0.95}$) were synthesized following the procedures reported previously.[54] The molar stoichiometry Ce:Zr of both MOFs determined by ICP analysis was 0.43:0.57 and 0.04:0.96, respectively. Moreover, the basic characterization of these materials, including X-Ray Diffraction (see Figure S1), TG analysis (see Figure S2) and N_2 adsorption (see Figure S3), correlates well with the literature data (see the Supporting Information for characterization details). Even though EPR presented a clear $O_2^{\cdot-}$ signal for the UiO-66(Ce) sample, UiO-66($Ce_{0.5}Zr_{0.5}$) and UiO-66($Ce_{0.05}Zr_{0.95}$) materials showed a flat baseline. Moreover, XPS spectra, previously controversial due to possible charging effects contribution, was barely observable for UiO-66($Ce_{0.5}Zr_{0.5}$) and undetectable for UiO-66($Ce_{0.05}Zr_{0.95}$) (see Figure S6). In all these cases, the employed techniques face a compromise between the amount of Ce^{3+} respect to the total Ce (lower than pure UiO-66(Ce)) and the detection limit of instrument.

Contrarily, UV-Vis spectra (see Figure S8) presented the same (reversible) absorption edge red-shift after Ce/Zr-MOFs thermal activation as previously reported for UiO-66(Ce). Moreover, the decrease on the band gap corroborates the Ce^{3+} increment during the activation (Figure S8 insets). This highlights that despite of lower Ce content, UV-Vis spectroscopy still allows to probe electronic bands variations induced by Ce^{3+} formation.

Finally, the hybrid materials have been characterized by CO adsorption followed by FTIR spectroscopy (see SI for details). Interestingly, even when we decrease dramatically the amount of cerium, the band at 2127 cm^{-1}, above suggested to originate from CO-Ce^{3+} interaction, is still clearly observable, testifying that in this sample a substantial portion of the Ce present is accessible and reduced (see Figure S9). Moreover, when the amount of Zr was increased

the band at 2127 cm^{-1} is now more stable during the evacuation process. This stability could be related to the Ce^{3+} dispersion in the catalyst. Indeed, it was demonstrated by Lomachenko and coworkers the presence of isolated Ce atoms on the Zr clusters with Ce<17%.[53] This suggests as in pure UiO-66(Ce), the CO-Ce^{3+} might be weaker due to Ce^{3+} dispersed among mostly Ce^{4+}. Contrarily on UiO-66($Ce_{0.05}Zr_{0.95}$) with Ce≈5% the CO-Ce^{3+} interaction is stronger (see inset in Figure S9) since Ce is introduced on (μ_3-OH)$CeZr_5$ cluster having then important applications as metal support or in catalysis.[55,56]

4. Conclusions

In summary, the employment of different hand able techniques showed as UV-Vis is generally the most accessible/reliable technique to qualitatively verify Ce^{3+} formation. XPS, even being efficient to detect and quantify Ce^{3+} in pure UiO-66(Ce), is not sufficiently sensitive for UiO-66(Ce/Zr) samples. While, UV-Vis and XPS are able to provide direct evidence of Ce^{3+}, FTIR and EPR have been used to prove Ce indirectly. CO band at 2127 cm^{-1}, which is assigned to Ce^{3+}-CO adduct, is clearly visible also in the sample with a very diluted amount of cerium e.g., UiO-66($Ce_{0.05}Zr_{0.95}$). Finally, as far as we could verify, we have reported for the first-time *operando* Ce M_5-edge NEXAFS to determine and quantify the amount of Ce^{3+} species formed during the UiO-66(Ce) dehydration. These species could be re-oxidized simply by an ambient exposure, doing the Ce^{3+}/Ce^{4+} interconversion reversible. This finding opens a new opportunity to apply these hybrid materials as metal support or in catalysis.

CRediT author statement

Sergio Rojas-Buzo: Supervision, Conceptualization, Methodology, Synthesis, Investigation, Formal analysis, Writing-Original draft preparation, **Davide Salusso:** Investigation, Writing-Original draft preparation, Formal analysis, **Francesca Bonino:** Supervision, Writing- Reviewing and Editing Resources, **Maria Cristina Paganini:** Writing- Reviewing and Editing Resources, Investigation, **Silvia Bordiga:** Conceptualization, Methodology, Visualization, Formal analysis, Supervision, Writing- Reviewing and Editing.

Appendix A. Supplementary data

Supplementary data to this article can be found online at https://doi.org/

5. ACKNOWLEDGMENTS

The authors are thankful to S. Mauri and M. L. R. Salazar from APE-HE (Elettra Synchrotron) for support with NEXAFS measurements. Dr. M. Signorile and G. Deplano are also acknowledged for support with NEXAFS measurements. S. Rojas-Buzo acknowledges the Margarita Salas grant financed by the Ministerio de Universidades, Spain, and also funded by the European Union-Next Generation EU.

6. REFERENCES

[1] A. Corma, H.I. Garcia, F.X. Llabrés i Xamena, Engineering metal organic frameworks for heterogeneous catalysis, Chem. Rev. 110 (2010) 4606–4655.

[2] H. Furukawa, K.E. Cordova, M. O'Keeffe, O.M. Yaghi, The Chemistry and Applications of Metal-Organic Frameworks, Science (80-.). 341 (2013) 1230444. https://www.sciencemag.org/lookup/doi/10.1126/science.1230444.

[3] L. Zhu, X.-Q. Liu, H.-L. Jiang, L.-B. Sun, Metal–organic frameworks for heterogeneous basic catalysis, Chem. Rev. 117 (2017) 8129–8176.

[4] Q. Wang, D. Astruc, State of the art and prospects in metal–organic framework (MOF)-based and MOF-derived nanocatalysis, Chem. Rev. 120 (2019) 1438–1511.

[5] A.J. Howarth, Y. Liu, P. Li, Z. Li, T.C. Wang, J.T. Hupp, O.K. Farha, Chemical, thermal and mechanical stabilities of metal–organic frameworks, Nat. Rev. Mater. 1 (2016) 1–15.

[6] M. Ding, X. Cai, H.-L. Jiang, Improving MOF stability: approaches and applications, Chem. Sci. 10 (2019) 10209–10230.

[7] H. Furukawa, F. Gandara, Y.-B. Zhang, J. Jiang, W.L. Queen, M.R. Hudson, O.M. Yaghi, Water adsorption in porous metal–organic frameworks and related materials, J. Am. Chem. Soc. 136 (2014) 4369–4381.

[8] S.B. Kalidindi, S. Nayak, M.E. Briggs, S. Jansat, A.P. Katsoulidis, G.J. Miller, J.E. Warren, D. Antypov, F. Corà, B. Slater, Chemical and structural stability of zirconium-based metal–organic frameworks with large three-dimensional pores by linker engineering, Angew. Chemie Int. Ed. 54 (2015) 221–226.

[9] T.-F. Liu, D. Feng, Y.-P. Chen, L. Zou, M. Bosch, S. Yuan, Z. Wei, S. Fordham, K. Wang, H.-C. Zhou,

Topology-guided design and syntheses of highly stable mesoporous porphyrinic zirconium metal–organic frameworks with high surface area, J. Am. Chem. Soc. 137 (2015) 413–419.

[10] D. Feng, K. Wang, J. Su, T. Liu, J. Park, Z. Wei, M. Bosch, A. Yakovenko, X. Zou, H. Zhou, A highly stable zeotype mesoporous zirconium metal–organic framework with ultralarge pores, Angew. Chemie Int. Ed. 54 (2015) 149–154.

[11] J.H. Cavka, S. Jakobsen, U. Olsbye, N. Guillou, C. Lamberti, S. Bordiga, K.P. Lillerud, A New Zirconium Inorganic Building Brick Forming Metal Organic Frameworks with Exceptional Stability, J. Am. Chem. Soc. 130 (2008) 13850–13851. https://doi.org/10.1021/ja8057953.

[12] J. Winarta, B. Shan, S.M. Mcintyre, L. Ye, C. Wang, J. Liu, B. Mu, A decade of UiO-66 research: a historic review of dynamic structure, synthesis mechanisms, and characterization techniques of an archetypal metal–organic framework, Cryst. Growth Des. 20 (2019) 1347–1362.

[13] J. Jacobsen, A. Ienco, R. D'Amato, F. Costantino, N. Stock, The chemistry of Ce-based metal-organic frameworks, Dalt. Trans. 49 (2020) 16551–16586. https://doi.org/10.1039/d0dt02813d.

[14] Z. Hu, Y. Wang, D. Zhao, The chemistry and applications of hafnium and cerium (iv) metal–organic frameworks, Chem. Soc. Rev. (2021).

[15] M. Lammert, C. Glißmann, H. Reinsch, N. Stock, Synthesis and characterization of new Ce (IV)-MOFs exhibiting various framework topologies, Cryst. Growth Des. 17 (2017) 1125–1131.

[16] R. D'Amato, A. Donnadio, M. Carta, C. Sangregorio, D. Tiana, R. Vivani, M. Taddei, F. Costantino, Water-based synthesis and enhanced CO2 capture performance of perfluorinated cerium-based metal–organic frameworks with UiO-66 and MIL-140 topology, ACS Sustain. Chem. Eng. 7 (2018) 394–402.

[17] T.J.M.M. Ntep, H. Reinsch, J. Liang, C. Janiak, Acetylenedicarboxylate-based cerium (IV) metal–organic framework with fcu topology: A potential material for air cleaning from toxic halogen vapors, Dalt. Trans. 48 (2019) 15849–15855.

[18] Y. Song, Y. Pi, X. Feng, K. Ni, Z. Xu, J.S. Chen, Z. Li, W. Lin, Cerium-based metal–organic layers catalyze hydrogen evolution reaction through dual photoexcitation, J. Am. Chem. Soc. 142 (2020) 6866–6871.

[19] T. Montini, M. Melchionna, M. Monai, P. Fornasiero, Fundamentals and catalytic applications of CeO2-based

materials, Chem. Rev. 116 (2016) 5987–6041.

[20] M. Lammert, M.T. Wharmby, S. Smolders, B. Bueken, A. Lieb, K.A. Lomachenko, D. De Vos, N. Stock, Cerium-based metal organic frameworks with UiO-66 architecture: Synthesis, properties and redox catalytic activity, Chem. Commun. 51 (2015) 12578–12581. https://doi.org/10.1039/c5cc02606g.

[21] S. Smolders, K.A. Lomachenko, B. Bueken, A. Struyf, A.L. Bugaev, C. Atzori, N. Stock, C. Lamberti, M.B.J. Roeffaers, D.E. De Vos, Unravelling the Redox-catalytic Behavior of Ce4+ Metal–Organic Frameworks by X-ray Absorption Spectroscopy, ChemPhysChem. 19 (2018) 373–378.

[22] S. Rojas-Buzo, P. Concepción, J.L. Olloqui-Sariego, M. Moliner, A. Corma, Metalloenzyme-Inspired Ce-MOF Catalyst for Oxidative Halogenation Reactions, ACS Appl. Mater. Interfaces. 13 (2021) 31021–31030. https://doi.org/10.1021/acsami.1c07496.

[23] M. Karimi, H. Mohebali, S. Sadeghi, V. Safarifard, A. Mahjoub, A. Heydari, Additive-free aerobic CH oxidation through a defect-engineered Ce-MOF catalytic system, Microporous Mesoporous Mater. 322 (2021) 111054.

[24] J. Yang, L. Chen, W. Li, G. Chen, L. Wang, S. Zhao, A novel self-supported structure of Ce-UiO-66/TNF in a redox electrolyte with high supercapacitive performance, J. Colloid Interface Sci. 573 (2020) 55–61. https://doi.org/10.1016/j.jcis.2020.03.115.

[25] Y. Zhang, X. Zeng, X. Jiang, H. Chen, Z. Long, Ce-based UiO-66 metal-organic frameworks as a new redox catalyst for atomic spectrometric determination of Se(VI) and colorimetric sensing of Hg(II), Microchem. J. 149 (2019) 103967. https://doi.org/10.1016/j.microc.2019.103967.

[26] C. Atzori, K.A. Lomachenko, S. Øien-Ødegaard, C. Lamberti, N. Stock, C. Barolo, F. Bonino, Disclosing the properties of a new Ce (III)-Based MOF: Ce2 (NDC) 3 (DMF) 2, Cryst. Growth Des. 19 (2018) 787–796.

[27] L.R. Redfern, M. Ducamp, M.C. Wasson, L. Robison, F.A. Son, F.-X. Coudert, O.K. Farha, Isolating the Role of the Node-Linker Bond in the Compression of UiO-66 Metal–Organic Frameworks, Chem. Mater. 32 (2020) 5864–5871. https://doi.org/10.1021/acs.chemmater.0c01922.

[28] E. Paparazzo, Corrigendum: Use and mis-use of x-ray photoemission Ce3d spectra of Ce 2 O 3 and CeO 2 (2018 J. Phys.: Condens. Matter 30 343003) , J. Phys. Condens. Matter. 32 (2020) 099501.

https://doi.org/10.1088/1361-648x/ab5763.

[29] C. Castán-Guerrero, D. Krizmancic, V. Bonanni, R. Edla, A. Deluisa, F. Salvador, G. Rossi, G. Panaccione, P. Torelli, A reaction cell for ambient pressure soft x-ray absorption spectroscopy, Rev. Sci. Instrum. 89 (2018). https://doi.org/10.1063/1.5019333.

[30] L. Braglia, M. Fracchia, P. Ghigna, A. Minguzzi, D. Meroni, R. Edla, M. Vandichel, E. Ahlberg, G. Cerrato, P. Torelli, Understanding Solid-Gas Reaction Mechanisms by Operando Soft X-Ray Absorption Spectroscopy at Ambient Pressure, J. Phys. Chem. C. 124 (2020) 14202–14212. https://doi.org/10.1021/acs.jpcc.0c02546.

[31] M. Fracchia, P. Ghigna, T. Pozzi, U. Anselmi Tamburini, V. Colombo, L. Braglia, P. Torelli, Stabilization by Configurational Entropy of the Cu(II) Active Site during CO Oxidation on Mg0.2Co0.2Ni0.2Cu0.2Zn0.2O, J. Phys. Chem. Lett. 11 (2020) 3589–3593. https://doi.org/10.1021/acs.jpclett.0c00602.

[32] D.H. Simonne, A. Martini, M. Signorile, A. Piovano, L. Braglia, P. Torelli, E. Borfecchia, G. Ricchiardi, THORONDOR: A software for fast treatment and analysis of low-energy XAS data, J. Synchrotron Radiat. 27 (2020) 1741–1752. https://doi.org/10.1107/S1600577520011388.

[33] J. Jaumot, R. Gargallo, A. De Juan, R. Tauler, A graphical user-friendly interface for MCR-ALS: A new tool for multivariate curve resolution in MATLAB, Chemom. Intell. Lab. Syst. 76 (2005) 101–110. https://doi.org/10.1016/j.chemolab.2004.12.007.

[34] M.J. Cliffe, W. Wan, X. Zou, P.A. Chater, A.K. Kleppe, M.G. Tucker, H. Wilhelm, N.P. Funnell, F.X. Coudert, A.L. Goodwin, Correlated defect nanoregions in a metal-organic framework, Nat. Commun. 5 (2014) 1–8. https://doi.org/10.1038/ncomms5176.

[35] X. Feng, H.S. Jena, C. Krishnaraj, D. Arenas-Esteban, K. Leus, G. Wang, J. Sun, M. Rüscher, J. Timoshenko, B. Roldan Cuenya, S. Bals, P. Van Der Voort, Creation of Exclusive Artificial Cluster Defects by Selective Metal Removal in the (Zn, Zr) Mixed-Metal UiO-66, J. Am. Chem. Soc. 143 (2021) 21511–21518. https://doi.org/10.1021/jacs.1c05357.

[36] B. Shan, S.M. McIntyre, M.R. Armstrong, Y. Shen, B. Mu, Investigation of Missing-Cluster Defects in UiO-66 and Ferrocene Deposition into Defect-Induced Cavities, Ind. Eng. Chem. Res. 57 (2018) 14233–14241. https://doi.org/10.1021/acs.iecr.8b03516.

[37] G.C. Shearer, S. Chavan, S. Bordiga, S. Svelle, U. Olsbye, K.P. Lillerud, Defect Engineering: Tuning the Porosity and Composition of the Metal–Organic Framework UiO-66 via Modulated Synthesis, Chem. Mater. 28 (2016) 3749–3761. https://pubs.acs.org/doi/10.1021/acs.chemmater.6b00602.

[38] F.G. Cirujano, N. Martin, L.H. Wee, Design of Hierarchical Architectures in Metal-Oganic Frameworks for Catalysis and Adsorption, Chem. Mater. 32 (2020) 10268–10295. https://doi.org/10.1021/acs.chemmater.0c02973.

[39] L. Liu, Z. Chen, J. Wang, D. Zhang, Y. Zhu, S. Ling, K.W. Huang, Y. Belmabkhout, K. Adil, Y. Zhang, B. Slater, M. Eddaoudi, Y. Han, Imaging defects and their evolution in a metal–organic framework at sub-unit-cell resolution, Nat. Chem. 11 (2019) 622–628. https://doi.org/10.1038/s41557-019-0263-4.

[40] T. Islamoglu, D. Ray, P. Li, M.B. Majewski, I. Akpinar, X. Zhang, C.J. Cramer, L. Gagliardi, O.K. Farha, From Transition Metals to Lanthanides to Actinides: Metal-Mediated Tuning of Electronic Properties of Isostructural Metal-Organic Frameworks, Inorg. Chem. 57 (2018) 13246–13251. https://doi.org/10.1021/acs.inorgchem.8b01748.

[41] D.M. Driscoll, D. Troya, P.M. Usov, A.J. Maynes, A.J. Morris, J.R. Morris, Geometry and energetics of CO adsorption on hydroxylated UiO-66, Phys. Chem. Chem. Phys. 21 (2019) 5078–5085. https://doi.org/10.1039/c8cp07778a.

[42] B. Villoria-del-Álamo, S. Rojas-Buzo, P. García-García, A. Corma, Zr-MOF-808 as Catalyst for Amide Esterification, Chem. - A Eur. J. 27 (2021) 4588–4598. https://doi.org/10.1002/chem.202003752.

[43] B. Bohigues, S. Rojas-Buzo, M. Moliner, A. Corma, Coordinatively Unsaturated Hf-MOF-808 Prepared via Hydrothermal Synthesis as a Bifunctional Catalyst for the Tandem N-Alkylation of Amines with Benzyl Alcohol, ACS Sustain. Chem. Eng. 9 (2021) 15793–15806. https://doi.org/10.1021/acssuschemeng.1c04903.

[44] C. Binet, M. Daturi, J.C. Lavalley, IR study of polycrystalline ceria properties in oxidised and reduced states, Catal. Today. 50 (1999) 207–225. https://doi.org/10.1016/S0920-5861(98)00504-5.

[45] B. Choudhury, A. Choudhury, Ce 3+ and oxygen vacancy mediated tuning of structural and optical properties of CeO 2 nanoparticles, Mater. Chem. Phys. 131 (2012) 666–671. https://doi.org/10.1016/j.matchemphys.2011.10.032.

[46] L. Wang, F. Meng, Oxygen vacancy and Ce3+ ion dependent magnetism of monocrystal CeO2 nanopoles synthesized by a facile hydrothermal method, Mater. Res. Bull. 48 (2013) 3492–3498. https://doi.org/10.1016/j.materresbull.2013.05.036.

[47] C. Ma, J. Fu, J. Chen, Y. Wen, P.O. Fasan, H. Zhang, N. Zhang, J. Zheng, B.H. Chen, Improving the Surface Properties of CeO2 by Dissolution of Ce3+ to Enhance the Performance for Catalytic Wet Air Oxidation of Phenol, Ind. Eng. Chem. Res. 56 (2017) 9090–9097. https://doi.org/10.1021/acs.iecr.7b02121.

[48] S. Méndez-Salazar, O. Aguilar-Martínez, Y. Piña-Pérez, R. Pérez-Hernández, C.E. Santolalla-Vargas, R. Gómez, F. Tzompantzi, Effect of the Oxygen Vacancies in CeO2 by the Ce3+ Incorporation to Enhance the Photocatalytic Mineralization of Phenol, ChemistrySelect. 6 (2021) 3435–3443. https://doi.org/10.1002/slct.202100459.

[49] P. Patsalas, S. Logothetidis, L. Sygellou, S. Kennou, Structure-dependent electronic properties of nanocrystalline cerium oxide films, Phys. Rev. B - Condens. Matter Mater. Phys. 68 (2003) 1–13. https://doi.org/10.1103/PhysRevB.68.035104.

[50] E. Cerrato, C. Gionco, M.C. Paganini, E. Giamello, E. Albanese, G. Pacchioni, Origin of Visible Light Photoactivity of the CeO2/ZnO Heterojunction, ACS Appl. Energy Mater. 1 (2018) 4247–4260. https://doi.org/10.1021/acsaem.8b00887.

[51] C. Gionco, E. Giamello, L. Mino, M.C. Paganini, The interaction of oxygen with the surface of CeO2-TiO2 mixed systems: An example of fully reversible surface-to-molecule electron transfer, Phys. Chem. Chem. Phys. 16 (2014) 21438–21445. https://doi.org/10.1039/c4cp03195d.

[52] S. Livraghi, M.C. Paganini, E. Giamello, G. Di Liberto, S. Tosoni, G. Pacchioni, Formation of Reversible Adducts by Adsorption of Oxygen on Ce-ZrO2: An Unusual I•2 Ionic Superoxide, J. Phys. Chem. C. 123 (2019) 27088–27096. https://doi.org/10.1021/acs.jpcc.9b08615.

[53] K.A. Lomachenko, J. Jacobsen, A.L. Bugaev, C. Atzori, F. Bonino, S. Bordiga, N. Stock, C. Lamberti, Exact Stoichiometry of Ce x Zr 6-x Cornerstones in Mixed-Metal UiO-66 Metal-Organic Frameworks Revealed by Extended X-ray Absorption Fine Structure Spectroscopy, J. Am. Chem. Soc. 140 (2018) 17379–17383. https://doi.org/10.1021/jacs.8b10343.

[54] M. Lammert, C. Glißmann, N. Stock, Tuning the stability of bimetallic Ce(iv)/Zr(iv)-based MOFs with UiO-66 and MOF-808 structures, Dalt. Trans. 46 (2017) 2425–2429. https://doi.org/10.1039/c7dt00259a.

[55] R. Kopelent, J.A. van Bokhoven, J. Szlachetko, J. Edebeli, C. Paun, M. Nachtegaal, O. V. Safonova, Catalytically Active and Spectator Ce 3+ in Ceria-Supported Metal Catalysts , Angew. Chemie. 127 (2015) 8852–8855. https://doi.org/10.1002/ange.201503022.

[56] S.D. Senanayake, P.J. Ramírez, I. Waluyo, S. Kundu, K. Mudiyanselage, Z. Liu, Z. Liu, S. Axnanda, D.J. Stacchiola, J. Evans, J.A. Rodriguez, Hydrogenation of CO2 to Methanol on CeOx/Cu(111) and ZnO/Cu(111) Catalysts: Role of the Metal-Oxide Interface and Importance of Ce3+ Sites, J. Phys. Chem. C. 120 (2016) 1778–1784. https://doi.org/10.1021/acs.jpcc.5b12012.